Thermal conductivity and internal temperature profiles of Li-ion secondary batteries

Frank Richter[a], Signe Kjelstrup[a], Preben J. S. Vie[b], Odne S. Burheim[c,*]

[a]*Department of Chemistry, Norwegian University of Science and Technology, NO-7491 Trondheim, Norway*
[b]*Institute for Energy Technology, Instituttveien 18, NO-2007 Kjeller, Norway*
[c]*Department of Energy and Process Engineering, Norwegian University of Science and Technology, NO-7491 Trondheim, Norway*

Abstract

In this paper we report the thermal conductivity for several battery components. Materials were obtained from several electrode- and separator suppliers, and some were extracted from commercial batteries. We measured with and without electrolyte solvent and at different compaction pressures. The experimentally obtained values are used in a thermal model and corresponding internal temperature profiles are shown. The thermal conductivity of dry separator materials was found to range from 0.07 ± 0.01 to 0.18 ± 0.02 $\mathrm{WK^{-1}m^{-1}}$. Dry electrode (active) materials ranged from 0.13 ± 0.02 to 0.61 ± 0.02 $\mathrm{WK^{-1}m^{-1}}$. Adding the electrolyte solvent increased the thermal conductivity of electrode (active) materials by at least a factor of 2.

Keywords: thermal conductivity measurements, temperature profile, thermal modelling, Li-ion battery

1. Introduction

Li-ion batteries have seen a major introduction to small scale hybrid and fully electric vehicles. As larger battery cells have become cheaper, Li-ion based batteries are currently seeing an introduction to large scale electric and hybrid electric vehicles [1], *e.g.*electric buses, hybrid electric buses and hybrid electric ships [2]. As larger vehicles take batteries into use, larger battery packs are needed, and more intense cycles are applied. Therefore, thermal management becomes more important, both internally and externally. The growing use of Li-ion batteries is not only due to their zero emission characteristic during operation and their rather low carbon footprint [3]. It has also been shown, that a more cost efficient application can be realized [2] but the specific energy of the battery is still a limiting factor, when we compare to gasoline-driven vehicles [4].

Fast charging of LIBs would require a good understanding of heat production and heat transfer within the battery. Effects like capacity fade, power fade, and self discharge within Li-ion batteries are well reported in the literature, *e.g.* by Bandhauer *et al.* [5]. Especially the temperature influence on different ageing mechanisms is well reported [6–9].

*Corresponding author: burheim@ntnu.no
Email addresses: frank.richter@ntnu.no (Frank Richter), signe.kjelstrup@ntnu.no (Signe Kjelstrup), preben.vie@ife.no (Preben J. S. Vie), burheim@ntnu.no (Odne S. Burheim)

Performance and cycle life are also dependent on battery design [10, 11], which will influence current distribution, state of charge (SOC), temperature and voltage distribution. This will influence local temperatures [12] and therefore, local degradation (ageing).

As a result, a correct determination and allocation of heat sources together with the thermal conductivities of the different components will allow modelling of internal temperature profiles. This can help a cooling system outside the battery or outside the battery pack. Moreover, improved thermal management will improve the understanding of local ageing mechanism and may lead to better battery designs and enhanced lifetimes. We find reports of several researchers using an *in-situ* measurement setup [13–16] to determine internal temperatures.

Finally, knowing internal temperature profiles at high current densities gives the possibility to predict and avoid conditions for thermal runaway, which is a key safety need for LIBs during operation at high current densities. One can see temperature behaviour of LIBs during thermal runaway in the publication of Wu *et al.* [17] who used an accelerated rate calorimeter technique. They showed the increase in temperature of a $LiCoO_2$|C and a $LiFePO_4$|C battery when exposed to high temperatures (> 100 °C).

Thermal conductivities of all components are key parameters for the modelling of temperature profiles. The materials' thermal conductivity is not necessarily isotropic. Usually, the terms "in-plane" and "cross-plane" are used. If we imagine a thin electrode, we differentiate between the direction perpendicular (cross-plane) and parallel to the plane (in-plane). There are reports on thermal conductivities of Li-ion secondary battery materials [18], but they are not thoroughly investigated [5]. In particular, there is not that many reports on thermal conductivity of separators. In the literature, we find values for separators, but these values vary from 0.33–1.29 $WK^{-1}m^{-1}$ [19–22]. Some of these values are assumed and there are almost no reports on the experimental determination of the cross-plane thermal conductivity of a separator. We found one paper from Vishwakarma and Jain [23], in which a transient DC heating method was used to obtain an in-plane thermal conductivity of a separator of 0.5 ± 0.03 $WK^{-1}m^{-1}$. Since the heat production is predominant in the separator-electrolyte region and to some extend within the solid electrolyte interface region at high currents [18], knowledge of the thermal conductivity of the electrolyte soaked separator is critical. In addition, temperature profiles of batteries will vary during operation, in terms of ageing, SOC and C-rate. Internal resistances are reported to increase during ageing [24–26], and this will influence the heat production inside the battery. In addition, the thermal conductivity of the graphite electrodes is reported to change for different graphite particle sizes, the relative amounts of polyvinylidene difluoride binder and carbon-black, and for different compaction pressures [27]. Last, the thermal conductivity is a function of temperature [27, 28]. Using photothermal deflection spectroscopy, Logos *et al.* reported the thermal conductivity for different commercial electrodes and find a decrease of 0.025–0.045 $WK^{-1}m^{-1}$ per Kelvin for different negative electrodes and 0.005–0.050 $WK^{-1}m^{-1}$ per Kelvin for different positive electrodes.

In this paper we report the thermal conductivity for a wide range of pristine materials at different compaction pressures, dry, and soaked in electrolyte solvent. Thereafter, we use an already developed simple 1-dimensional thermal model [18] to compare these values and put them into a thermal context.

2. Experimental

2.1. Apparatus - thermal conductivity measurements

The thermal conductivity meter is presented in Fig. 1. It is explained in detail by Burheim *et. al* [29]. It measures the temperature at different equidistant places in the stainless steel cylinders, the temperature drop over the sample and the thickness of the sample. The thermal conductivity of the stainless steel was known, which made it possible to compute the heat flux through the system.

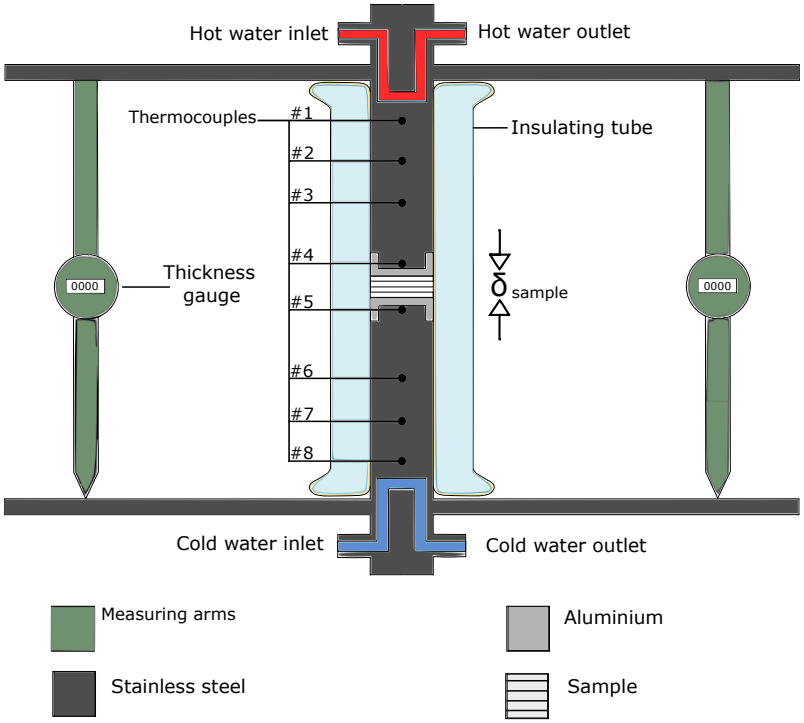

Figure 1: The thermal conductivity meter, which measures thickness and temperature drop over the sample and the temperature drop over the stainless steel cylinders.

The average sample temperature was close to room temperature, because of a lower temperature of 10 °C and a higher temperature of 35 °C on the bottom and the top of the thermal conductivity meter, respectively. Measurements were carried out at compaction pressures of 2.3 bar, 4.6 bar 6.9 bar, 9.2 bar and 11.5 bar. When measuring electrolyte solvent soaked samples, materials were soaked in a 50:50 vol.% mixture of diethyl carbonate and ethylen carbonate without the presence of $LiPF_6$. As one can see later, this does not significantly effect the thermal conductivity of the examined separator or the NMC-cathode, but an effect on the thermal conductivity of the graphite-anode of up to about 35 % increase was measured.

2.2. Materials

We investigated separators from Viledon®, Celgard®, and Whatman. Table 1 gives an overview of all separators, their materials, and their impregnation (in case of the separators from Viledon®).

Table 1: Overview of investigated separators and their materials.

Manufact.	**Designation**	**Material**	Impregnation
Viledon®	FS 3002-23	Polyethylene terephthalate	Al_2O_3
Viledon®	FS 3005-25	Polyethylene terephthalate	Al_2O_3
Viledon®	FS 3001-30	Polyethylene terephthalate	Al_2O_3
Viledon®	FS 3006-25	Polyethylene terephthalate	Al_2O_3, AlO(OH)
Celgard®	2400	Polypropylene	
Whatman	1823070	Glass microfibers	

In addition, we investigated a $LiFePO_4$ electrode from MTI Corporation (bc-af-241lpf-ss), and $LiCoO_2$ (HS-LIB-P-Co-001) and graphite (HS-LIB-N-Gr-001) electrodes from Hohsen Corporation. Finally, we investigated materials from a commercial battery (XALT31HE, MODEL F910-0006), which had a nominal capacity of 31 Ah. The battery materials from XALT were measured after the disassembling of the battery and after cleaning them from remaining $LiPF_6$ salt.

3. Theory

3.1. Thermal conductivity measurements

The total thermal resistance R_{sample}, which is the sum of the thermal resistance of the sample and its contact resistance $R_{\text{apparatus–sample}}$ with the apparatus, were plotted as a function of sample thickness and the thermal conductivity was obtained as the inverse of the slope. Different thicknesses were achieved by stacking of samples. In case of electrodes, the thermal resistance of the sample had two contributions, the thermal resistance of the active material $\frac{\delta_{\text{act.M.}}}{k_{\text{act.M.}}}$ and the thermal resistance of the current collector $\frac{\delta_{\text{foil}}}{k_{\text{foil}}}$. Both contributions can be expressed by their respective thickness δ divided by their thermal conductivity k. It was shown before [24], that the total thermal resistance can be calculated by using the temperature drop over the sample and the heat flux q_{sample} through the sample.

$$R_{\text{sample}} = \frac{T_4 - T_5}{q_{\text{sample}}} = 2R_{\text{apparatus–sample}} + \frac{\delta_{\text{act.M.}}}{k_{\text{act.M.}}} + \frac{\delta_{\text{foil}}}{k_{\text{foil}}} \tag{1}$$

It was also shown, that additional contact resistances from stacking can be neglected [29]. The term $\delta_{\text{foil}}/\text{k}_{\text{foil}}$ in equation 1, which refers to the current collectors, equals zero in case separators, and can be neglected in case of electrodes [24].

3.2. Internal heat production

There are three heat sources within a Li-ion secondary battery: ohmic heat production, heat production or consumption due to the entropy change of the electrode reactions (reversible heat production) and heat production from the resistance of the electrochemical reaction. All heat sources were discussed in [24] and the total heat generation at charge and discharge of a LIB as a whole can be described as follows:

$$q_{\mathrm{ch}} = \left(+ \frac{T \Delta_{dch} S}{F} j + r_{\omega} j^2 + \eta j \right) \tag{2}$$

$$q_{\mathrm{disch}} = \left(- \frac{T \Delta_{dch} S}{F} j + r_{\omega} j^2 + \eta j \right) \tag{3}$$

$j, r_{\omega}, T, \Delta_{dch} S, F, \eta$ refer to current density, ohmic resistance, temperature, entropy change of the whole cell, Faraday constant, and overpotential. The equations 2 and 3 use different signs for the reversible heat production. We define $\Delta_{dch} S$ as the change in entropy during the discharge process. The dependency of the heat production on the state of charge is neglected. In particular, we use an averaged value for the entropy change.

3.3. 1D modelling of the internal temperature profile

To indicate the impact of the thermal conductivity values, we used them in a simple model [29]. A pouch cell was modelled with isothermal boundary conditions. The housing of the pouch cell was neglected and only the electrodes and separator were modelled. The volumetric heat production Q_{eff} for n cells during charge and discharge, was obtained using equations 2 and 3, respectively.

$$Q_{\mathrm{eff}} = \frac{q}{d_{\mathrm{total}}} \cdot \frac{n}{2} \tag{4}$$

d_{total} is the total thickness of the battery. An effective thermal conductivity k_{eff} was used which was calculated by weighting the electrodes and the separator by their thickness d_{i}:

$$k_{\mathrm{eff}} = \frac{d_{\mathrm{total}}}{\sum \frac{d_{\mathrm{i}}}{k_{\mathrm{i}}}} \tag{5}$$

We consider, that heat transfer perpendicular to the surface of the pouch cells predominates. Hence, Fourier's second law in one dimension (cross plane to the pouch cell) can be applied.

$$\frac{d^2 T}{dx^2} = \frac{-Q_{\mathrm{eff}}}{k_{\mathrm{eff}}} = \alpha \tag{6}$$

The maximum temperature in the centre of the battery at an ambient temperature of T_0 becomes [30]:

$$T_{\mathrm{max}}|_{\mathrm{x=0}} = -\frac{\alpha d_{total}^2}{8} + T_0 \tag{7}$$

4. Results and discussion

4.1. Thermal conductivity

The measured effective thermal conductivities of the electrodes and separators and the calculated values for the active materials only are given in Table 2 and Table 3.

Table 2: Thermal conductivity for electrolyte solvent soaked and dry separators and electrodes at a compaction pressure of 2.3 bar.

Manuf.	**Material**	$k^{\mathrm{d}}_{\mathrm{electrode}}$/ W K^{-1}m^{-1}	$k^{\mathrm{s}}_{\mathrm{electrode}}$/ W K^{-1}m^{-1}	$k^{\mathrm{d}}_{\mathrm{a.m.}}$/ W K^{-1}m^{-1}	$k^{\mathrm{s}}_{\mathrm{a.m.}}$/ W K^{-1}m^{-1}
Viledon®	Sep. FS 3002-23			0.14 ± 0.03	0.36 ± 0.03
Viledon®	Sep. FS 3005-25			0.12 ± 0.01	0.36 ± 0.02
Viledon®	Sep. FS 3001-30			0.10 ± 0.04	0.31 ± 0.02
Viledon®	Sep. FS 3006-25			0.12 ± 0.02	0.28 ± 0.01
Celgard®	Sep. 2400			0.07 ± 0.01	0.14 ± 0.03
Whatman	Filter 1823070			0.12 ± 0.04	0.19 ± 0.01
MTI	LFP electrode bc-af-241lpf-ss	0.15 ± 0.02	0.36 ± 0.01	0.13 ± 0.02	0.32 ± 0.01
Hohsen	LCO electrode HS-LIB-P-Co-001	0.25 ± 0.02	1.51 ± 0.12	0.17 ± 0.02	1.03 ± 0.09
Hohsen	Graph. electrode HS-LIB-N-Gr-001	0.34 ± 0.01	1.45 ± 0.02	0.26 ± 0.01	1.11 ± 0.02

[d]dry – no electrolyte solvent,[s]soaked in electrolyte solvent,[a.m.]active material,

[electrode] whole electrode, including active material and current collector

Table 3: Thermal conductivity for electrolyte solvent soaked and dry separators and electrodes at a compaction pressure of 11.5 bar.

Manuf.	**Material**	$k^{\mathrm{d}}_{\mathrm{electrode}}$/ W K^{-1}m^{-1}	$k^{\mathrm{s}}_{\mathrm{electrode}}$/ W K^{-1}m^{-1}	$k^{\mathrm{d}}_{\mathrm{a.m.}}$/ W K^{-1}m^{-1}	$k^{\mathrm{s}}_{\mathrm{a.m.}}$/ W K^{-1}m^{-1}
Viledon®	Sep. FS 3002-23			0.17 ± 0.02	0.39 ± 0.01
Viledon®	Sep. FS 3005-25			0.18 ± 0.02	0.40 ± 0.02
Viledon®	Sep. FS 3001-30			0.14 ± 0.04	0.36 ± 0.04
Viledon®	Sep. FS 3006-25			0.13 ± 0.01	0.30 ± 0.01
Celgard®	Sep. 2400			0.07 ± 0.01	0.10 ± 0.02
Whatman	Filter 1823070			0.08 ± 0.02	0.20 ± 0.02
MTI	LFP electrode bc-af-241lpf-ss	0.17 ± 0.01	0.39 ± 0.02	0.15 ± 0.01	0.36 ± 0.02
Hohsen	LCO electrode HS-LIB-P-Co-001	0.38 ± 0.02	2.17 ± 0.11	0.26 ± 0.01	1.48 ± 0.08
Hohsen	Graph. electrode HS-LIB-N-Gr-001	0.68 ± 0.02	1.80 ± 0.20	0.52 ± 0.02	1.38 ± 0.16

$^{\mathrm{d}}$dry – no electrolyte solvent,$^{\mathrm{s}}$soaked in electrolyte solvent,$^{\mathrm{a.m.}}$active material,

$^{\mathrm{electrode}}$ whole electrode, including active material and current collector

Soaked samples showed a significantly higher thermal conductivity. While graphite and LCO from Hohsen showed a higher dependency on electrolyte solvent soaking, the effect was a factor of about 2 for the separators from Viledon®. The factor 3 for graphite was in very good agreement with [31]. When comparing the dependency on the compaction pressure, we found that the graphite electrode from Hohsen showed a higher dependency than the LCO electrode from Hohsen, while for both porous materials, the pressure dependency of dry and soaked samples is comparable with values for micro porous layers used in fuel cells. [32, 33]. All separators showed a low compaction pressure dependency on the thermal conductivity - comparable to Hauge *et al.* [34]. The separator from Celgard® showed the lowest thermal conductivity at all compaction pressures.

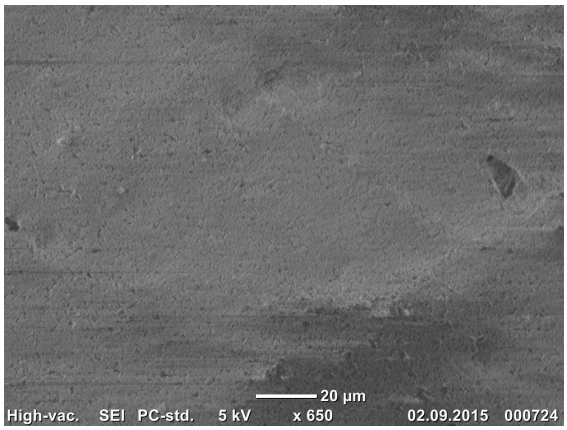

(a) Viledon® separator FS 3002-23

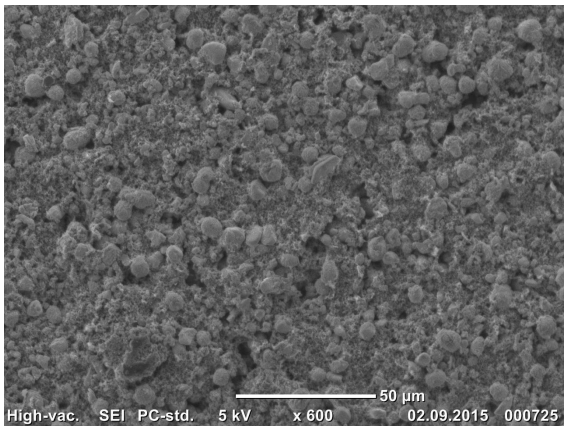

(b) Hohsen LCO electrode HS-LIB-P-Co-001

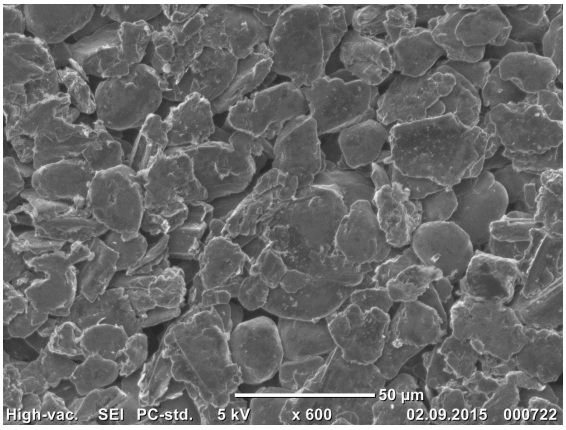

(c) Hohsen graphite electrode HS-LIB-N-Gr-001

Figure 2: SEM images of some of the investigated materials.

While the separator showed an increase in thermal conductivity of a factor of about 2 after soaking with electrolyte solvent, graphite and LCO increased with a factor of about 3-5 depending on the compaction pressure. The dependence of the thermal conductivity on pressure could be explained by a more rough structure and more space for the electrolyte solvent, see Figure 2.

Tables 4 and 5 give the thermal conductivity values at 2.3 and 11.5 bar compaction pressure for the XALT battery materials. The graphite electrode shows very similar thermal conductivities like the graphite electrode from Hohsen at the dry state at 2.3 and 11.5 bar compaction pressure. When soaked with electrolyte solvent, the graphite electrode from Hohsen shows a thermal conductivity which is about 50 % higher than XALT. The thermal conductivity of the electrolyte solvent soaked NMC electrode and the separator from the XALT battery do not show a dependency whether they are cleaned from the $LiPF_6$ salt before the measurement or not.

Table 4: Thermal conductivity for electrolyte solvent soaked and dry materials from a commercial XALT battery at a compaction pressure of 2.3 bar.

Manuf.	**Material**	$k^{\mathrm{d}}_{\mathrm{electrode}}$/ W $\mathrm{K^{-1}m^{-1}}$	$k^{\mathrm{s}}_{\mathrm{electrode}}$/ W $\mathrm{K^{-1}m^{-1}}$	$k^{\mathrm{d}}_{\mathrm{a.m.}}$/ W $\mathrm{K^{-1}m^{-1}}$	$k^{\mathrm{s}}_{\mathrm{a.m.}}$/ W $\mathrm{K^{-1}m^{-1}}$
XALT	Graph. electrode	0.37 ± 0.03	1.04 ± 0.02	0.32 ± 0.03	0.89 ± 0.01
XALT	Graph. electrode*		1.39 ± 0.07		1.18 ± 0.06
XALT	NMC electrode	0.40 ± 0.06	0.99 ± 0.05	0.30 ± 0.05	0.82 ± 0.04
XALT	NMC electrode*		1.06 ± 0.09		0.88 ± 0.07
XALT	Separator			0.09 ± 0.01	0.21 ± 0.06
XALT	Separator*				0.22 ± 0.02

$^{\mathrm{d}}$dry – no electrolyte solvent,$^{\mathrm{s}}$soaked in electrolyte solvent,$^{\mathrm{a.m.}}$active material,

$^{\mathrm{electrode}}$ whole electrode, including active material and current collector

* not cleaned from the $LiPF_6$ salt

Table 5: Thermal conductivity for electrolyte solvent soaked and dry materials from a commercial XALT battery at a compaction pressure of 11.5 bar.

Manuf.	**Material**	$k^{\mathrm{d}}_{\mathrm{electrode}}$/ W $\mathrm{K^{-1}m^{-1}}$	$k^{\mathrm{s}}_{\mathrm{electrode}}$/ W $\mathrm{K^{-1}m^{-1}}$	$k^{\mathrm{d}}_{\mathrm{a.m.}}$/ W $\mathrm{K^{-1}m^{-1}}$	$k^{\mathrm{s}}_{\mathrm{a.m.}}$/ W $\mathrm{K^{-1}m^{-1}}$
XALT	Graph. electrode	0.71 ± 0.07	1.60 ± 0.03	0.61 ± 0.06	1.37 ± 0.02
XALT	Graph. electrode*		2.01 ± 0.22		1.72 ± 0.19
XALT	NMC electrode	0.47 ± 0.02	1.08 ± 0.04	0.39 ± 0.02	0.90 ± 0.04
XALT	NMC electrode*		1.09 ± 0.10		0.91 ± 0.08
XALT	Separator			0.10 ± 0.01	0.23 ± 0.05
XALT	Separator*				0.24 ± 0.02

$^{\mathrm{d}}$dry – no electrolyte solvent,$^{\mathrm{s}}$soaked in electrolyte solvent,$^{\mathrm{a.m.}}$active material,

$^{\mathrm{electrode}}$ whole electrode, including active material and current collector

* not cleaned from the $LiPF_6$ salt

The values in Table 2 and Table 4 will be used for modelling. Tables showing the thermal conductivity values of all materials at 4.6 bar, 6.9 bar, and 9.2 bar can be found in the appendix. Figures 3 and 4 give the thermal conductivities for a selection of the materials as a function of compaction pressure, for the dry state and soaked with electrolyte solvent, respectively.

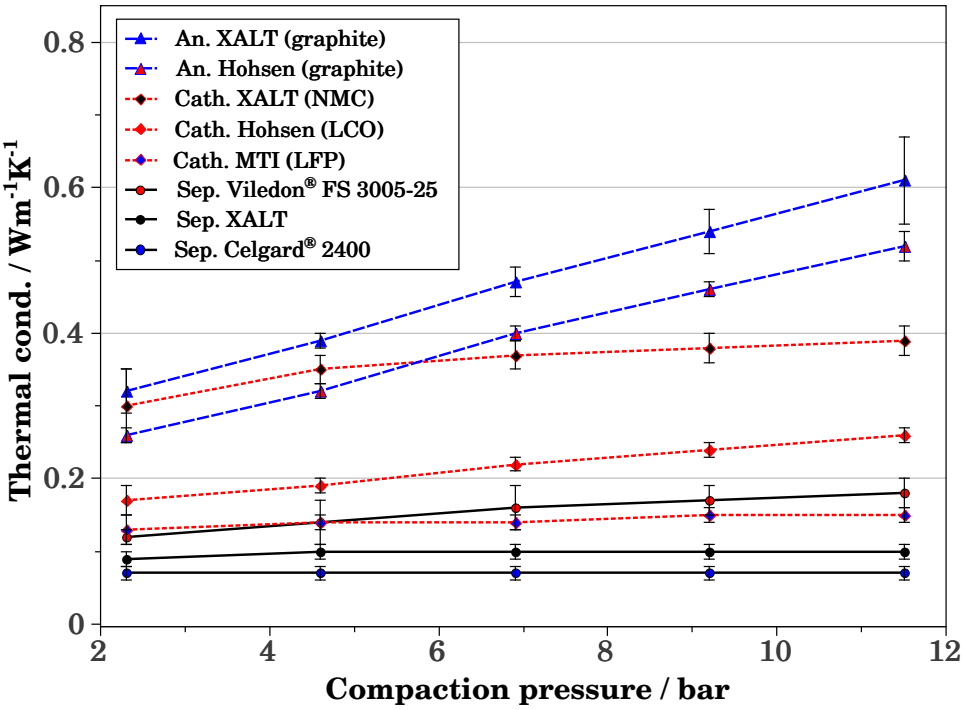

Figure 3: The thermal conductivity of the dry XALT battery components, the separators Viledon®FS 3005-25 and Celgard®2400, an LCO and a graphite electrode from Hohsen, and a LFP electrode from MTI as function of compaction pressure. Separators are drawn in black lines, cathodes in red lines, and anodes in blue lines.

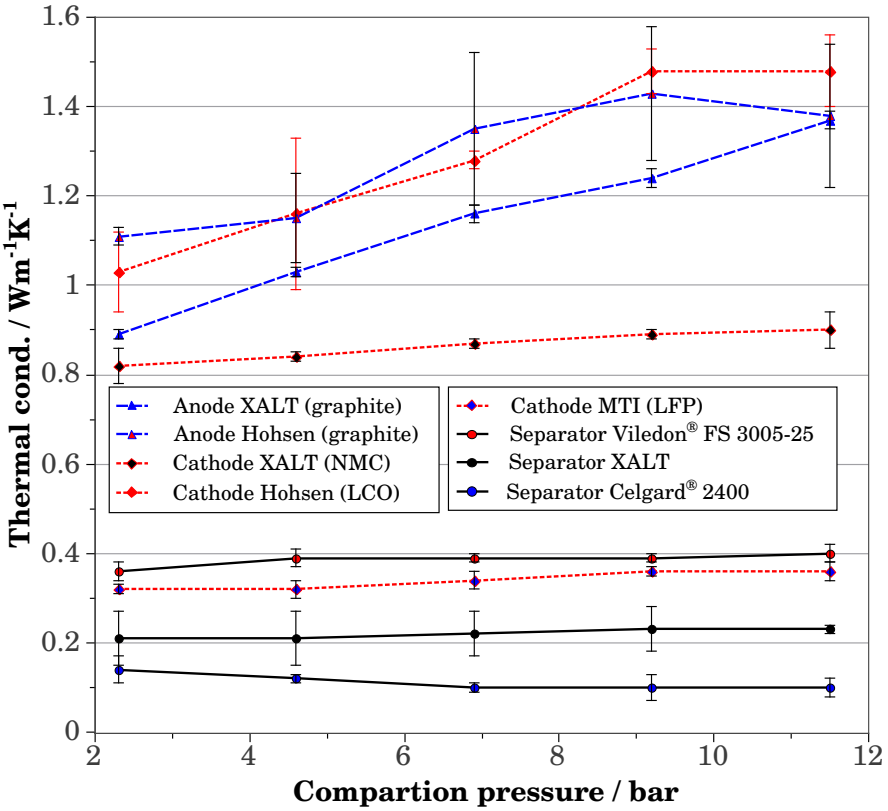

Figure 4: The thermal conductivity of the electrolyte soaked XALT battery components, the separators Viledon®FS 3005-25 and Celgard®2400, an LCO and a graphite electrode from Hohsen, and a LFP electrode from MTI as function of compaction pressure. Separators are drawn in black lines, cathodes in red lines, and anodes in blue lines.

4.2. Temperature profile assessment

In order to use equations 2 and 3, we need the entropy change of the electrode reaction, the specific ohmic resistance and the overpotential from the Tafel equation. We used an entropy change of $-9\frac{\mathrm{J}}{\mathrm{mol \cdot K}}$ [35] for the NMC | graphite cell. According to Burheim *et al.* [18], we assumed an ohmic resistance of $2\mathrm{m\Omega \cdot m^2}$ and an overpotential of $\eta = -0.042 + 0.067 \cdot \log(\mathrm{j})$. A stack of 34 cells was modelled. The thickness of the Cu current collector, Al current collector, positive electrode active material, negative electrode active material and separator were 25, 28, 67, 74, and 13 μm respectively. The thermal conductivity values can be found in Table 4. We modelled without the presence of $LiPF_6$ and neglected the influence of temperature on the thermal conductivity.

Fig. 5 shows the temperature profile for 10C, 6C and 2C discharge rates, which correspond to discharge or charging times of a full or empty battery within 6 min, 10 min and 30 min, respectively. Although a discharge rate of 10C is out of question for most of the graphite electrodes, we found a temperature difference of about 5.5 K from the edge to the center with perfect isothermal boundary conditions.

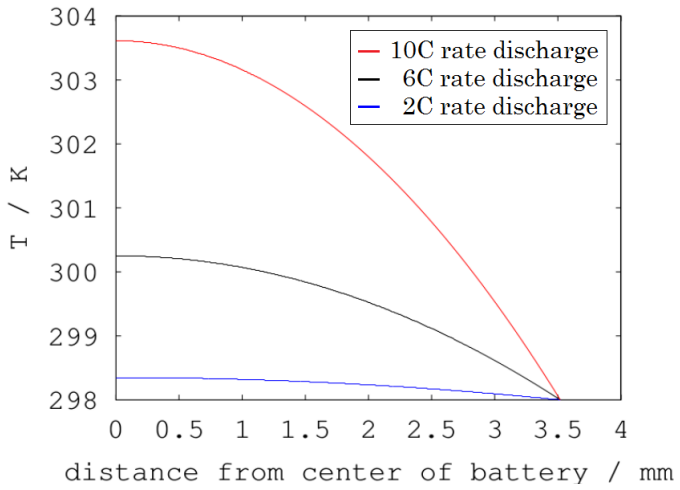

Figure 5: The 1D temperature profile cross-plane an NMC | graphite cell for 2C (blue), 6C (black), and 10C (red) discharge current

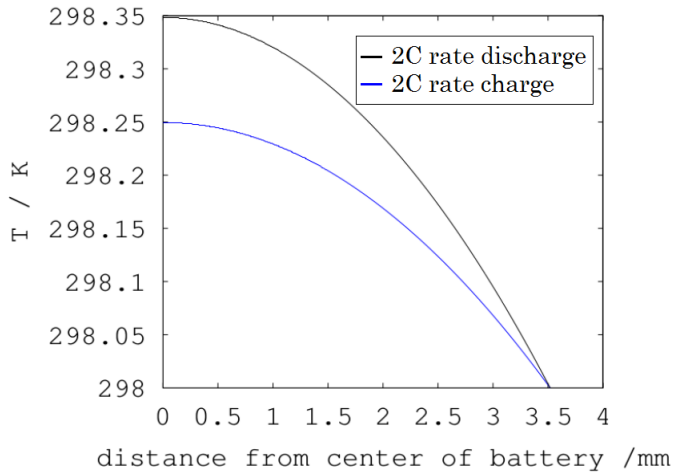

Figure 6: The 1D temperature profile cross-plane an NMC | graphite cell for 2C discharge (black) and 2C charge (blue) current

Fig. 6 shows the temperature difference between the edge of the battery and the centre for the same stack of 34 cells for a discharge and charge rate of 2C. We found a temperature difference in the center of about 0.1 K, comparing charging and discharging of the battery. Since the entropic heat is linearly dependent on the current density, we would find about 0.3 K and 0.5 K difference between charge and discharge in the center, for a 6C discharge rate and 10C discharge rate, respectively.

Finally, we modelled different cell chemistries and show their influence on the maximum temperature rise in the centre of the battery. To be able to do so, we kept the thickness of the components constant and used the same XALT separator for all cells (see Table 4, $k^{s}_{\text{a.m.}} = 0.21\ \text{Wm}^{-1}\text{K}^{-1}$). In addition to the NMC | graphite cell, which we modelled

before, we showed the maximum temperature rise as function of the C-rate (discharge) of an LCO | graphite cell (overall entropy change of $-35\frac{\mathrm{J}}{\mathrm{mol{\cdot}K}}$[35]) and a LFP | graphite cell (overall entropy change of $-9\frac{\mathrm{J}}{\mathrm{mol{\cdot}K}}$[35]). In case of the LFP | graphite and the LCO | graphite cell, we used the graphite anode from Hohsen. To show the importance of the thermal conductivity of the separator, we finally calculated the maximum temperature in the centre of the battery for the same cell chemistries, using $k^{s}_{\mathrm{a.m.}} = 1\ \mathrm{Wm^{-1}K^{-1}}$ for the separator like Kim *et al.* [21]. The results are given in Figure 7.

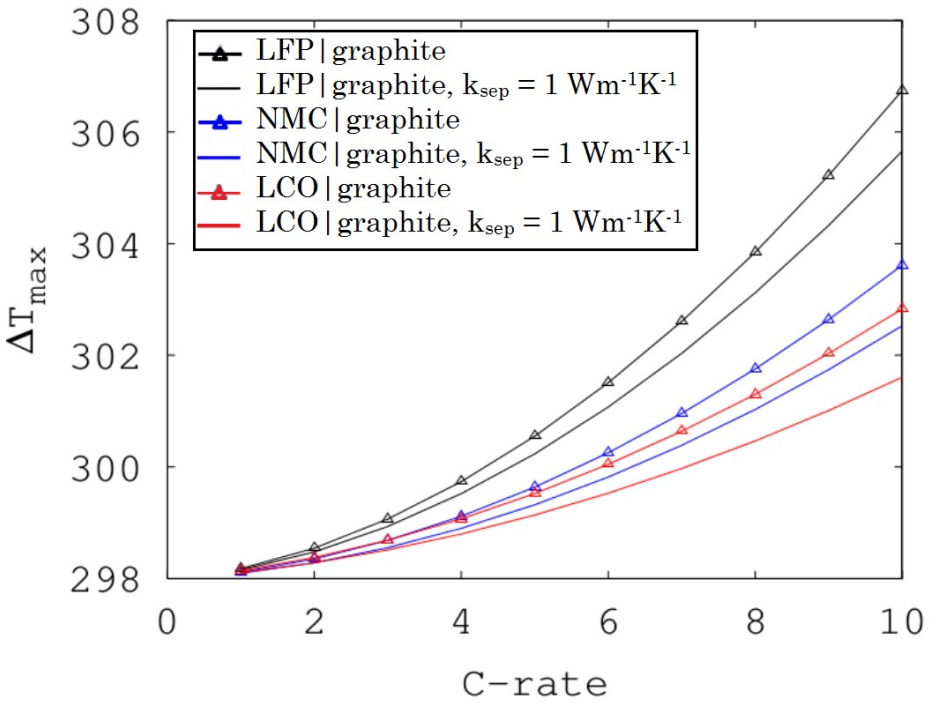

Figure 7: The maximum temperature in the centre of the battery as function of the C-rate (discharge) for an NMC | graphite cell from XALT (blue), an LFP(MTI) | graphite(Hohsen) cell (black) and an LCO(Hohsen) | graphite(Hohsen) cell (red). The graphs without the triangle are calculated using a thermal conductivity of the separator of 1 $\mathrm{Wm^{-1}K^{-1}}$ [21].

As we can see in Figure 7, the maximum temperature rise as a function of discharge C-rate is similar for the NMC | graphite cell from XALT and the LCO | graphite cell (both materials from Hohsen). The overall entropy change for LCO—graphite ($-35\frac{\mathrm{J}}{\mathrm{mol{\cdot}K}}$) is significantly higher than for NMC | graphite ($-9\frac{\mathrm{J}}{\mathrm{mol{\cdot}K}}$). But LCO and graphite from Hohsen have higher thermal conductivities (see Tables 2 and 4). Due to the much lower thermal conductivity of the LFP, the temperature rise is significantly higher for the LFP | graphite cell. At a discharge rate of 10C, we find a difference of more than 8 K from the edge to the center. Using the higher thermal conductivity for the separator of 1 $\mathrm{Wm^{-1}K^{-1}}$ [21] the effective thermal conductivity of the whole cell (see equation 5) increased and, therefore, lowered the maximum temperature. Table 6 showes the effective thermal conductivities for the batteries modelled in Fig. 7.

When considering internal temperature profiles beyond current rates of ±2-3 C, there are 3 major factors influencing the maximum temperature rise in the pouch cell. First, ΔT_{max} is proportional to the current density by the power of 2.

Second, there is a linearity to internal resistance, which is a function of ageing. It can increase by a factor of 2 from 100–80 % state of health [24]. Last, there is thermal conductivities, to which the maximum temperature is inversely proportional. It is well known that, electrolyte is decomposing during ageing [7]. Although even aged electrodes close to 0 % SOH should not be dried out completely, dry electrodes would increase the maximum temperature rise at least by a factor of 2. This means that going from 2C to 4C (factor 4) and from pristine to aged cells at 80 % SOH (at least factor 2), the maximum temperature in a pouch cell will increase by a factor of at least 8.

Table 6: Effective thermal conductivity of the batteries modelled in Fig. 7

Separator	XALT (see Table 4)	Separator used by Kim *et al.* [21]
Cell chemistry	$k_{\mathrm{eff,XALT}}$ / $\mathrm{WK^{-1}m^{-1}}$	$k_{\mathrm{eff,Kim}}$ / $\mathrm{WK^{-1}m^{-1}}$
NMC(XALT) | graphite (XALT)	0.82	1.01
LFP(MTI) | graphite(Hohsen)	0.53	0.60
LCO(Hohsen) | graphite(Hohsen)	1.07	1.44

5. Conclusion

We have measured the thermal conductivity of commercial electrodes of $LiCoO_2$ and graphite from Hohsen Corp., $LiFePO_4$ from MTI Corp., four commercial separators from Viledon® (Freudenberg), one separator from Celgard® and a micro fibre glass filter from Whatman.

The thermal conductivity of the dry cathodes ranged from 0.13 to 0.47 $\mathrm{WK^{-1}m^{-1}}$ while the dry anodes ranged from 0.34 to 0.71 $\mathrm{WK^{-1}m^{-1}}$. Adding electrolyte solvent increased the thermal conductivity of the electrodes at least by a factor of 2 (for $LiFePO_4$ electrodes) up to a maximal factor of 6 (for $LiCoO_2$ electrodes). Dry separators ranged from 0.07 to 0.18 $\mathrm{WK^{-1}m^{-1}}$ and adding electrolyte solvent increased the thermal conductivity by factors of 1.5 to 3.

In addition, the thermal conductivities of both electrodes and separator from a XALT 31HE cell were measured, which were then used as parameters in a model for the internal temperature distribution.

Furthermore, we modelled a $LiFePO_4$ | graphite and an $LiCoO_2$ | graphite cell as function of the current density, using the geometry of the same cell. We found that the maximum temperature in the centre of the battery is similar for the LiNiMnCo | graphite and the $LiCoO_2$ | graphite cell, while it is significantly higher for the $LiFePO_4$ | graphite cell. This difference gets even larger at higher current densities.

Acknowledgements

We acknowledge the Research Council of Norway (project no. 228739) for funding through the project ”Life and Safety for Li-ion batteries in Maritime conditions (SafeLiLife)”.

[1] B. G. Pollet, I. Staffell, J. L. Shang, Current status of hybrid, battery and fuel cell electric vehicles: From electrochemistry to market prospects, Electrochimica Acta 84 (2012) 235 – 249, {ELECTROCHEMICAL} {SCIENCE} {AND} {TECHNOLOGYState} of the Art and Future PerspectivesOn the occasion of the International Year of Chemistry (2011). doi:http://dx.doi.org/10.1016/j.electacta.2012.03.172.
URL //www.sciencedirect.com/science/article/pii/S0013468612005671

[2] B. J. Vartdal, C. Chryssakis, Potential benefits of hybrid powertrain systems for various ship types, in: International Scientific Conference on Hybrid and Electric Vehcicles, 2011, pp. 1–12.

[3] G. Saevarsdottir, P. Tao, H. Stefansson, W. Harvey, Potential use of geothermal energy sources for the production of lithium-ion batteries, Renewable Energy 61 (2014) 17 – 22, World Renewable Energy Congress Sweden, 813 May, 2011, Linköping, Sweden. doi:http://dx.doi.org/10.1016/j.renene.2012.04.028.
URL http://www.sciencedirect.com/science/article/pii/S0960148112002698

[4] T. Mayer, D. Kreyenberg, J. Wind, F. Braun, Feasibility study of 2020 target costs for PEM fuel cells and lithium-ion batteries: A two-factor experience curve approach, International Journal of Hydrogen Energy 37 (19) (2012) 14463 – 14474, HYFUSENSpecial Issue for the 4th National - 3rd Latin American Conference on Hydrogen and Sustainable Energy Sources (HYFUSEN), 6-9 June 2011, Mar Del Plata, Argentina. doi:http://dx.doi.org/10.1016/j.ijhydene.2012.07.022.
URL http://www.sciencedirect.com/science/article/pii/S0360319912015972

[5] T. M. Bandhauer, S. Garimella, T. F. Fuller, A critical review of thermal issues in Lithium-Ion batteries, Journal of The Electrochemical Society 158 (3) (2011) R1–R25. arXiv:http://jes.ecsdl.org/content/158/3/R1.full.pdf+html, doi:10.1149/1.3515880.
URL http://jes.ecsdl.org/content/158/3/R1.abstract

[6] M. Broussely, P. Biensan, F. Bonhomme, P. Blanchard, S. Herreyre, K. Nechev, R. Staniewicz, Main aging mechanisms in li ion batteries, Journal of Power Sources 146 (12) (2005) 90 – 96, Selected papers pressented at the 12th International Meeting on Lithium Batteries, 12th International Meeting on Lithium Batteries. doi:http://dx.doi.org/10.1016/j.jpowsour.2005.03.172.
URL http://www.sciencedirect.com/science/article/pii/S0378775305005082

[7] J. Vetter, P. Novák, M. Wagner, C. Veit, K.-C. Móller, J. Besenhard, M. Winter, M. Wohlfahrt-Mehrens, C. Vogler, A. Hammouche, Ageing mechanisms in lithium-ion batteries, Journal of Power Sources 147 (12) (2005) 269 – 281. doi:http://dx.doi.org/10.1016/j.jpowsour.2005.01.006.
URL http://www.sciencedirect.com/science/article/pii/S0378775305000832

[8] F. Leng, C. M. Tan, M. Pecht, Effect of temperature on the aging rate of li ion battery operating above room temperature, Scientific Reports 5 (2015) 12967 EP –.
URL http://dx.doi.org/10.1038/srep12967

[9] T. Waldmann, M. Wilka, M. Kasper, M. Fleischhammer, M. Wohlfahrt-Mehrens, Temperature dependent ageing mechanisms in Lithium-ion batteries a post-mortem study, Journal of Power Sources 262 (2014) 129 – 135. doi:http://dx.doi.org/10.1016/j.jpowsour.2014.03.112.
URL http://www.sciencedirect.com/science/article/pii/S0378775314004352

[10] G. Zhang, C. E. Shaffer, C.-Y. Wang, C. D. Rahn, Effects of non-uniform current distribution on energy density of Li-Ion cells, Journal of The Electrochemical Society 160 (11) (2013) A2299–A2305. arXiv:http://jes.ecsdl.org/content/160/11/A2299.full.pdf+html, doi:10.1149/2.061311jes.
URL http://jes.ecsdl.org/content/160/11/A2299.abstract

[11] J. Nanda, J. Remillard, A. O'Neill, D. Bernardi, T. Ro, K. E. Nietering, J.-Y. Go, T. J. Miller, Local state-of-charge mapping of lithium-ion battery electrodes, Advanced Functional Materials 21 (17) (2011) 3282–3290. doi:10.1002/adfm.201100157.
URL http://dx.doi.org/10.1002/adfm.201100157

[12] J. B. Robinson, J. A. Darr, D. S. Eastwood, G. Hinds, P. D. Lee, P. R. Shearing, O. O. Taiwo, D. J. Brett, Non-uniform temperature distribution in li-ion batteries during discharge a combined thermal imaging, x-ray micro-tomography and electrochemical impedance approach, Journal of Power Sources 252 (2014) 51 – 57. doi:http://dx.doi.org/10.1016/j.jpowsour.2013.11.059.
URL //www.sciencedirect.com/science/article/pii/S0378775313018867

[13] C. Heubner, C. Lämmel, N. Junker, M. Schneider, A. Michaelis, Microscopic in-operando thermography at the cross section of a single lithium ion battery stack, Electrochemistry Communications 48 (2014) 130 – 133. doi:http://dx.doi.org/10.1016/j.elecom.2014.09.007.
URL http://www.sciencedirect.com/science/article/pii/S138824811400294X

[14] C. Heubner, M. Schneider, C. Lämmel, U. Langklotz, A. Michaelis, In-operando temperature measurement across the interfaces of a lithium-ion battery cell, Electrochimica Acta 113 (2013) 730 – 734. doi:http://dx.doi.org/10.1016/j.electacta.2013.08.091.
URL http://www.sciencedirect.com/science/article/pii/S0013468613016216

[15] G. Zhang, L. Cao, S. Ge, C.-Y. Wang, C. E. Shaffer, C. D. Rahn, In situ measurement of radial temperature distributions in cylindrical Li-ion cells, Journal of The Electrochemical Society 161 (10) (2014) A1499–A1507. arXiv:http://jes.ecsdl.org/content/161/10/A1499.full.pdf+html, doi:10.1149/2.0051410jes.
URL http://jes.ecsdl.org/content/161/10/A1499.abstract

[16] C. Veth, D. Dragicevic, C. Merten, Thermal characterizations of a large-format lithium ion cell focused on high current discharges, Journal of Power Sources 267 (2014) 760 – 769. doi:http://dx.doi.org/10.1016/j.jpowsour.2014.05.139.
URL http://www.sciencedirect.com/science/article/pii/S0378775314008325

[17] Y.-F. Wu, D. Brun-Buisson, S. Genies, F. Mattera, J. Merten, Thermal behavior of Lithium-ion cells by adiabatic calorimetry: One of the selection criteria for all applications of storage, ECS Transactions 16 (29) (2009) 93–103. arXiv:http://ecst.ecsdl.org/content/16/29/93.full.pdf+html, doi:10.1149/1.3115311.
URL http://ecst.ecsdl.org/content/16/29/93.abstract

[18] O. S. Burheim, M. A. Onsrud, J. G. Pharoah, F. Vullum-Bruer, P. J. S. Vie, Thermal conductivity, heat sources and temperature profiles of Li-ion batteries, ECS Transactions 58 (48) (2014) 145–171.

[19] S. Chen, C. Wan, Y. Wang, Thermal analysis of lithium-ion batteries, Journal of Power Sources 140 (1) (2005) 111 – 124. doi:http://dx.doi.org/10.1016/j.jpowsour.2004.05.064.
URL http://www.sciencedirect.com/science/article/pii/S0378775304008596

[20] P. Taheri, M. Bahrami, Temperature rise in prismatic polymer lithium-ion batteries: An analytic approach, SAE Int. J. Passeng. Cars-Electron. Electr. Syst 5 (1) (2012) 164–176.

[21] U. S. Kim, C. B. Shin, C.-S. Kim, Modeling for the scale-up of a lithium-ion polymer battery, Journal of Power Sources 189 (1) (2009) 841 – 846, Selected Papers presented at the 14th International Meeting on Lithium Batteries (IMLB-2008). doi:http://dx.doi.org/10.1016/j.jpowsour.2008.10.019.
URL http://www.sciencedirect.com/science/article/pii/S0378775308019149

[22] W. Wu, X. Xiao, X. Huang, Modeling heat generation in a lithium ion battery, in: ASME 2011 5th International Conference on Energy Sustainability, American Society of Mechanical Engineers, 2011, pp. 1513–1522.

[23] V. Vishwakarma, A. Jain, Measurement of in-plane thermal conductivity and heat capacity of separator in Li-ion cells using a transient DC heating method, Journal of Power Sources 272 (2014) 378 – 385. doi:http://dx.doi.org/10.1016/j.jpowsour.2014.08.066.
URL http://www.sciencedirect.com/science/article/pii/S0378775314013214

[24] F. Richter, P. J. S. Vie, S. Kjelstrup, O. S. Burheim, Measurements of ageing and internal temperature profiles of secondary Li-ion secondary batteries and their impact on internal temperature profiles, submitted.

[25] A. Eddahech, O. Briat, J.-M. Vinassa, Performance comparison of four lithiumion battery technologies under calendar aging, Energy 84 (2015) 542 – 550. doi:http://dx.doi.org/10.1016/j.energy.2015.03.019.
URL http://www.sciencedirect.com/science/article/pii/S0360544215003138

[26] T. R. Tanim, C. D. Rahn, Aging formula for lithium ion batteries with solid electrolyte interphase layer growth, Journal of Power Sources 294 (2015) 239 – 247. doi:http://dx.doi.org/10.1016/j.jpowsour.2015.06.014.
URL http://www.sciencedirect.com/science/article/pii/S0378775315010484

[27] H. Maleki, J. R. Selman, R. B. Dinwiddie, H. Wang, High thermal conductivity negative electrode material for lithium-ion batteries, Journal of Power Sources 94 (1) (2001) 26 – 35. doi:http://dx.doi.org/10.1016/S0378-7753(00)00661-3.

URL http://www.sciencedirect.com/science/article/pii/S0378775300006613

[28] A. Loges, S. Herberger, D. Werner, T. Wetzel, Thermal characterization of Li-ion cell electrodes by photothermal deflection spectroscopy, Journal of Power Sources 325 (2016) 104 – 115. doi:http://dx.doi.org/10.1016/j.jpowsour.2016.05.082.
URL http://www.sciencedirect.com/science/article/pii/S0378775316306358

[29] O. Burheim, P. J. S. Vie, J. Pharoah, S. Kjelstrup, Ex situ measurements of through-plane thermal conductivities in a polymer electrolyte fuel cell, Journal of Power Sources 195 (1) (2010) 249 – 256. doi:http://dx.doi.org/10.1016/j.jpowsour.2009.06.077.
URL http://www.sciencedirect.com/science/article/pii/S0378775309011483

[30] R. B. Bird, W. E. Stewart, E. N. Lightfoot, Transport Phenomena, Revised 2nd Edition, Vol. 2, John Wiley & Sons, 2007.

[31] O. S. Burheim, M. Aslan, J. S. Atchison, V. Presser, Thermal conductivity and temperature profiles in carbon electrodes for supercapacitors, Journal of Power Sources 246 (2014) 160 – 166. doi:http://dx.doi.org/10.1016/j.jpowsour.2013.06.164.
URL http://www.sciencedirect.com/science/article/pii/S0378775313011774

[32] O. S. Burheim, H. Su, H. H. Hauge, S. Pasupathi, B. G. Pollet, Study of thermal conductivity of PEM fuel cell catalyst layers, International Journal of Hydrogen Energy 39 (17) (2014) 9397 – 9408. doi:http://dx.doi.org/10.1016/j.ijhydene.2014.03.206.
URL http://www.sciencedirect.com/science/article/pii/S0360319914009343

[33] O. S. Burheim, H. Su, S. Pasupathi, J. G. Pharoah, B. G. Pollet, Thermal conductivity and temperature profiles of the micro porous layers used for the polymer electrolyte membrane fuel cell, International Journal of Hydrogen Energy 38 (20) (2013) 8437 – 8447. doi:http://dx.doi.org/10.1016/j.ijhydene.2013.04.140.
URL http://www.sciencedirect.com/science/article/pii/S036031991301118X

[34] H. Hauge, V. Presser, O. Burheim, In-situ and ex-situ measurements of thermal conductivity of supercapacitors, Energy 78 (2014) 373 – 383. doi:http://dx.doi.org/10.1016/j.energy.2014.10.022.
URL http://www.sciencedirect.com/science/article/pii/S0360544214011712

[35] V. V. Viswanathan, D. Choi, D. Wang, W. Xu, S. Towne, R. E. Williford, J.-G. Zhang, J. Liu, Z. Yang, Effect of entropy change of lithium intercalation in cathodes and anodes on Li-ion battery thermal management, Journal of Power Sources 195 (11) (2010) 3720 – 3729.

Appendix A. additional thermal conductivity values

Table A.7, Table A.8, and Table A.9 show the thermal conductivity values for the components of the commercial battery for different compaction pressures.

Table A.7: Thermal conductivity for electrolyte solvent soaked and dry separators and electrodes at a compaction pressure of 4.6 bar.

Manuf.	**Material**	$k^{\mathrm{d}}_{\mathrm{electrode}}$/ W K^{-1}m^{-1}	$k^{\mathrm{s}}_{\mathrm{electrode}}$/ W K^{-1}m^{-1}	$k^{\mathrm{d}}_{\mathrm{a.m.}}$/ W K^{-1}m^{-1}	$k^{\mathrm{s}}_{\mathrm{a.m.}}$/ W K^{-1}m^{-1}
Viledon®	Sep. FS 3002-23			0.14 ± 0.03	0.37 ± 0.04
Viledon®	Sep. FS 3005-25			0.14 ± 0.03	0.39 ± 0.02
Viledon®	Sep. FS 3001-30			0.11 ± 0.02	0.32 ± 0.01
Viledon®	Sep. FS 3006-25			0.12 ± 0.01	0.29 ± 0.01
Celgard®	Sep. 2400			0.07 ± 0.01	0.12 ± 0.01
Whatman	Filter 1823070			0.09 ± 0.02	0.18 ± 0.02
MTI	LFP electrode bc-af-241lpf-ss	0.16 ± 0.01	0.36 ± 0.02	0.14 ± 0.01	0.32 ± 0.02
Hohsen	LCO electrode HS-LIB-P-Co-001	0.28 ± 0.02	1.70 ± 0.25	0.19 ± 0.01	1.16 ± 0.17
Hohsen	Graph. electrode HS-LIB-N-Gr-001	0.41 ± 0.02	1.50 ± 0.13	0.32 ± 0.01	1.15 ± 0.10
XALT	Graph. electrode	0.46 ± 0.02	1.20 ± 0.01	0.39 ± 0.01	1.03 ± 0.01
XALT	Graph. electrode*		1.46 ± 0.17		1.24 ± 0.14
XALT	NMC electrode	0.42 ± 0.02	1.01 ± 0.01	0.35 ± 0.02	0.84 ± 0.01
XALT	NMC electrode*		1.07 ± 0.08		0.89 ± 0.06
XALT	Separator			0.10 ± 0.01	0.21 ± 0.06
XALT	Separator*				0.23 ± 0.02

$^{\mathrm{d}}$dry – no electrolyte solvent,$^{\mathrm{s}}$soaked in electrolyte solvent,$^{\mathrm{a.m.}}$active material,

$^{\mathrm{electrode}}$ whole electrode, including active material and current collector

* not cleaned from the $LiPF_6$ salt

Table A.8: Thermal conductivity for electrolyte solvent soaked and dry separators and electrodes at a compaction pressure of 6.9 bar.

Manuf.	**Material**	$k^{\mathrm{d}}_{\mathrm{electrode}}$/ W K^{-1}m^{-1}	$k^{\mathrm{s}}_{\mathrm{electrode}}$/ W K^{-1}m^{-1}	$k^{\mathrm{d}}_{\mathrm{a.m.}}$/ W K^{-1}m^{-1}	$k^{\mathrm{s}}_{\mathrm{a.m.}}$/ W K^{-1}m^{-1}
Viledon®	Sep. FS 3002-23			0.15 ± 0.03	0.39 ± 0.04
Viledon®	Sep. FS 3005-25			0.16 ± 0.03	0.39 ± 0.01
Viledon®	Sep. FS 3001-30			0.12 ± 0.03	0.34 ± 0.06
Viledon®	Sep. FS 3006-25			0.12 ± 0.01	0.29 ± 0.01
Celgard®	Sep. 2400			0.07 ± 0.01	0.10 ± 0.01
Whatman	Filter 1823070			0.09 ± 0.01	0.19 ± 0.03
MTI	LFP electrode bc-af-241lpf-ss	0.16 ± 0.01	0.38 ± 0.02	0.14 ± 0.01	0.34 ± 0.02
Hohsen	LCO electrode HS-LIB-P-Co-001	0.32 ± 0.01	1.88 ± 0.03	0.22 ± 0.01	1.28 ± 0.02
Hohsen	Graph. electrode HS-LIB-N-Gr-001	0.51 ± 0.01	1.77 ± 0.22	0.40 ± 0.01	1.35 ± 0.17
XALT	Graph. electrode	0.55 ± 0.02	1.35 ± 0.01	0.47 ± 0.02	1.16 ± 0.01
XALT	Graph. electrode*		1.68 ± 0.15		1.43 ± 0.12
XALT	NMC electrode	0.45 ± 0.02	1.04 ± 0.01	0.37 ± 0.02	0.87 ± 0.01
XALT	NMC electrode*		1.09 ± 0.07		0.90 ± 0.06
XALT	Separator			0.10 ± 0.01	0.22 ± 0.05
XALT	Separator*				0.24 ± 0.02

$^{\mathrm{d}}$dry – no electrolyte solvent,$^{\mathrm{s}}$soaked in electrolyte solvent,$^{\mathrm{a.m.}}$active material,

$^{\mathrm{electrode}}$ whole electrode, including active material and current collector

* not cleaned from the $LiPF_6$ salt

Table A.9: Thermal conductivity for electrolyte solvent soaked and dry separators and electrodes at a compaction pressure of 9.2 bar

Manuf.	**Material**	$k^{\mathrm{d}}_{\mathrm{electrode}}$/ W K^{-1}m^{-1}	$k^{\mathrm{s}}_{\mathrm{electrode}}$/ W K^{-1}m^{-1}	$k^{\mathrm{d}}_{\mathrm{a.m.}}$/ W K^{-1}m^{-1}	$k^{\mathrm{s}}_{\mathrm{a.m.}}$/ W K^{-1}m^{-1}
Viledon®	Sep. FS 3002-23			0.16 ± 0.02	0.39 ± 0.04
Viledon®	Sep. FS 3005-25			0.17 ± 0.02	0.39 ± 0.01
Viledon®	Sep. FS 3001-30			0.13 ± 0.03	0.34 ± 0.06
Viledon®	Sep. FS 3006-25			0.13 ± 0.02	0.30 ± 0.01
Celgard®	Sep. 2400			0.07 ± 0.01	0.10 ± 0.03
Whatman	Filter 1823070			0.09 ± 0.02	0.19 ± 0.02
MTI	LFP electrode bc-af-241lpf-ss	0.17 ± 0.01	0.39 ± 0.01	0.15 ± 0.01	0.36 ± 0.01
Hohsen	LCO electrode HS-LIB-P-Co-001	0.36 ± 0.02	2.20 ± 0.07	0.24 ± 0.01	1.48 ± 0.05
Hohsen	Graph.electrode HS-LIB-N-Gr-001	0.60 ± 0.01	1.87 ± 0.19	0.46 ± 0.01	1.43 ± 0.15
XALT	Graph. electrode	0.63 ± 0.04	1.45 ± 0.03	0.54 ± 0.03	1.24 ± 0.02
XALT	Graph. electrode*		1.85 ± 0.19		1.58 ± 0.16
XALT	NMC electrode	0.46 ± 0.02	1.08 ± 0.01	0.38 ± 0.02	0.89 ± 0.01
XALT	NMC electrode*		1.09 ± 0.04		0.91 ± 0.03
XALT	Separator			0.10 ± 0.01	0.23 ± 0.05
XALT	Separator*				0.24 ± 0.02

$^{\mathrm{d}}$dry – no electrolyte solvent,$^{\mathrm{s}}$soaked in electrolyte solvent,$^{\mathrm{a.m.}}$active material,

$^{\mathrm{electrode}}$ whole electrode, including active material and current collector

* not cleaned from the $LiPF_6$ salt